Photonics-Assisted Radio Frequency Memory

Dan Zhu, *Member, IEEE*, Wenjuan Chen, Sijia Liu, Yue Yang, Jiang Liu, Xingwei Ye, *Student Member, IEEE*, Minghai Pan, and Shilong Pan, *Senior Member, IEEE*

***Abstract*—A radio frequency memory (RFM) based on microwave photonic mixing and digital RFM is proposed and demonstrated. By introducing the microwave photonic mixing, the operational frequency range is largely extended. Besides, the mixing spurs are effectively suppressed, which is important to guarantee the system efficiency and avoid generating significant feature for the jamming recognition. Meanwhile, by applying the digital RFM, flexible modulation and reconstruction are achieved. A proof-of-concept experiment is carried out. The wide working frequency range from C- to Ka- bands is achieved. The mixing spurs over the 0–40 GHz frequency range are experimentally suppressed. Radar imaging is successfully deceived. A radar waveform with a bandwidth of 500 MHz in the K band is successfully received and reconstructed. Two false targets are added. To the best of our knowledge, it is the first time that a photonics-assisted RFM is reported to have the functions of storage, flexible modulation, and reconstruction with wideband RF signals at a high frequency. The proposed scheme shows the great potential to be applied in electronic warfare, electronic environment simulation and testing, and so on.**

***Index Terms*—Microwave photonics, optical frequency conversion, optical memories, radio frequency.**

I. Introduction

RADIO frequency memory (RFM) realizes the functions of storing, modulating, restructuring, and retransmitting RF signals [1]. It has wide applications in the areas requiring analysis and flexible syntheses of RF and microwave signals, such as radar, electronic intelligence, electronic warfare, and electronic environment simulation and testing [2]–[4]. A typical RFM system is shown in Fig. 1. The input RF signal is firstly mixed with a local oscillator (LO) signal. The mixers can be sampling mixers [5], single-ended mixers [1], I/Q mixers [1], or double-balanced mixers [6], and so on. The generated intermediate frequency (IF) signal is then sampled at an analog to digital converter (ADC), stored, and restructured (e.g., time-delayed, frequency-shifted, or modulated by other signals) in the memory. After digital to analog conversion, the output signal is mixed with the LO, which is up-converted to the required frequency.

Two key parameters of the RFMs are the working frequency range and the spurious suppression ratio. With the development of the radar and electronic warfare systems towards high resolution, being intelligent, and being multifunctional [7], [8], the operation frequency increases rapidly. The investigations with RFMs are widely taken in recent years, aiming to improve the working frequency range and so on [9], [10]. However, electronic RFMs usually have a poor performance when operating at a high frequency or with large bandwidth. The instantaneous bandwidth of the commercial RFMs is limited to 1 to 2 GHz, and the operational frequency range is only several GHz [11], which cannot meet the requirements of future applications. Channelized methods have been investigated to increase the bandwidth of the RFM system, but the improvement is still limited [5], [12]. Besides, LO leakage and other mixing spurs would be generated in the electrical mixers or channelizers, which greatly degrade the performance of the system. These spurs will not only reduce the efficiency of the interference transmission, but also constitute a significant feature for the jamming recognition.

One possible solution to this challenge is microwave photonics [13]. A recirculating loop structure utilizing a fiber-optic delay line has been demonstrated as photonic RF memory [14], [15]. The RF signal to be stored is firstly modulated to the optical domain, which is then injected into the photonic recirculating loop to realize the storage function. By introducing an optical frequency shifter into the loop, the self-excitation problem is overcome. Multiple recirculations and long storage time are therefore enabled. However, only the storage function has been achieved. In [16], [17], the Doppler frequency shift function is added by introducing two acousto-optic modulators (AOMs). The RF signal to be operated is modulated to the optical domain with the carrier suppressed single-sideband modulation (CS-SSB) format, which is then frequency shifted by one AOM. The other AOM realizes the frequency shift of the optical carrier. By combing the two optical signals, the Doppler frequency shift is achieved. However, the instantaneous bandwidth of the optical signal that can be frequency shifted by the AOMs is limited to only tens of MHz. Thus the instantaneous bandwidth of the RF signal is limited to tens of MHz. Only the experimental results with RF signals having the single-tone frequency format are given in [16], [17]. It can be summarized that the necessary functions required for electronic warfare, multifunctional radars, and cognitive RF systems [18], such as modulation and reconstruction with wideband RF signals at high frequencies, have not been realized with the current photonics-based approaches.

Manuscript received February 4, 2021; revised June 26, 2021, August 17, 2021, and September 30, 2021; accepted October 16, 2021. Date of publication October 26, 2021; date of current version February 1, 2022. This work was supported in part by the National Natural Science Foundation of China under Grant 61971222 and in part by the Fundamental Research Fund for Central Universities under Grant NE2017002. *(Corresponding author: Shilong Pan.)*

The authors are with the College of Electronic and Information Engineering, Nanjing University of Aeronautics and Astronautics, Nanjing 210016, China (e-mail: danzhu@nuaa.edu.cn; cwj@nuaa.edu.cn; liusijia@nuaa.edu.cn; yangyue96@nuaa.edu.cn; 18251817898@nuaa.edu.cn; yexw@nuaa.edu.cn; panmh@nuaa.edu.cn; pans@ieee.org).

Color versions of one or more figures in this article are available at https://doi.org/10.1109/JLT.2021.3122141.

Digital Object Identifier 10.1109/JLT.2021.3122141

0733-8724 © 2021 IEEE. Personal use is permitted, but republication/redistribution requires IEEE permission.
See https://www.ieee.org/publications/rights/index.html for more information.

Authorized licensed use limited to: NANJING UNIVERSITY OF AERONAUTICS AND ASTRONAUTICS. Downloaded on February 17,2022 at 06:59:22 UTC from IEEE Xplore. Restrictions apply.

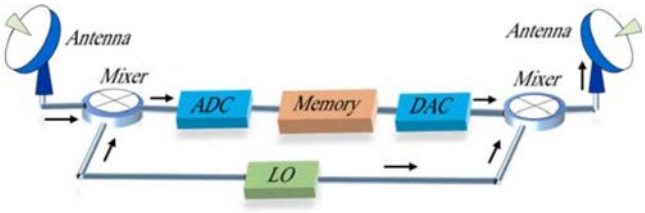

Fig. 1. Schematic diagram of a conventional RFM. RFM: radio frequency memory, ADC: analog to digital converter, LO: local oscillator, DAC: digital to analog converter.

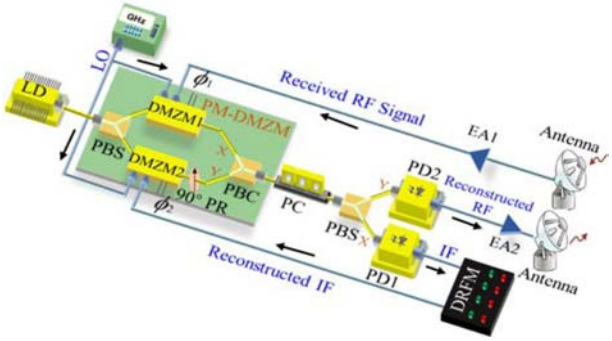

Fig. 2. Schematic diagram of the proposed photonics-assisted RFM. LD: laser diode; PM-DMZM: polarization-multiplexing dual-drive Mach Zehnder modulator; DMZM: dual-drive Mach-Zehnder modulator; PBS: polarization beam splitter; PR: polarization rotator; PC: polarization controller; PD: photodetector; PBC: polarization beam combiner; DRFM: digital radio frequency memory; EA: electrical amplifier.

In this paper, an RFM based on microwave photonic mixing is proposed and demonstrated to have the functions of storage, flexible modulation, and reconstruction. Through utilizing the polarization multiplexing technique, only a polarization-multiplexing dual-drive Mach Zehnder modulator (PM-DMZM) is needed. The wide working bandwidth and high working frequency are guaranteed, and the mixing spurs of the second harmonic IF components and the RF and LO leakages can be effectively eliminated by introducing the microwave photonic mixing. The flexible modulation and reconstruction operations are implemented by using the digital RFM. A proof-of-concept experiment is carried out. A radar waveform with a bandwidth of 500 MHz in the K band is successfully reconstructed by the proposed photonics-assisted RFM. Two false targets are experimentally obtained, and the radar imaging is deceived successfully.

II. Principle

The schematic diagram of the proposed photonics-assisted RFM is shown in Fig. 2. A continuous-wave (CW) light with a frequency of f_c is generated from a laser diode (LD). It is then injected into a PM-DMZM, which consists of two sub-DMZMs (DMZM1 and DMZM2) along two orthogonal polarization states. In the upper branch, the RF signal collected by the receiving antenna is amplified by an electrical amplifier (EA, EA1) and injected into one RF port of DMZM1. A LO signal with a frequency of f_L is injected into the other RF port of DMZM1. The RF signal could have different formats. Here, we take a linearly frequency modulated (LFM) waveform for an example, which can be expressed as $\mathrm{RF}(t) = \cos(2\pi f_0 t + \pi k t^2)$ $(0 < t < T)$, where f_0 is the initial frequency, k is chirp rate and T is the time duration. Considering the small signal modulation condition, by making DMZM1 biased at the minimum transmission point, only the $\pm 1^{\mathrm{st}}$ optical sidebands remain. The optical output of DMZM1 can be written as

$$\begin{aligned} E_x(t) &\propto e^{j2\pi f_c t}\left[e^{j\beta_1\cos\left(2\pi f_0 t+\pi k t^2\right)}\cdot e^{j\phi_1}+e^{j\beta_2\cos 2\pi f_L t}\right] \\ &\approx e^{j2\pi f_c t}\left[jJ_1(\beta_1)\,e^{-j\left(2\pi f_0 t+\pi k t^2\right)}\right. \\ &\quad \left.+\,jJ_1(\beta_1)\,e^{j\left(2\pi f_0 t+\pi k t^2\right)}\right] \\ &\quad +e^{j2\pi f_c t}\left[jJ_1(\beta_2)\,e^{-j2\pi f_L t}+jJ_1(\beta_2)\,e^{j2\pi f_L t}\right] \end{aligned} \tag{1}$$

where β_1 and β_2 are the modulation indices of the input RF and LO signals, respectively. A PC and a PBS are inserted after the PM-DMZM to split the optical signals along with two orthogonal polarization states. The optical signal output from DMZM1 is along the X-polarization axis, which will be output from one port of the PBS. When it is injected into a photodetector (PD, PD1), the electrical output is given as

$$\begin{aligned} i_x(t) \propto\ & {J_1}^2(\beta_2)\cos(4\pi f_L t)+{J_1}^2(\beta_1)\cos\left(4\pi f_0 t+2\pi k t^2\right) \\ & -J_1(\beta_1)J_1(\beta_2)\cos\left[2\pi(f_0+f_L)t+\pi k t^2\right] \\ & -J_1(\beta_1)J_1(\beta_2)\cos\left[2\pi(f_0-f_L)t+\pi k t^2\right] \end{aligned} \tag{2}$$

As can be seen, the RF and LO leakages are effectively suppressed. It should be noted that the second harmonic IF components will be generated from the beating between the $+2^{\mathrm{nd}}$ (or -2^{nd}) optically-carried RF sideband and $+2^{\mathrm{nd}}$ (or -2^{nd}) optically-carried LO sideband. Thus the second harmonic IF components will also be effectively eliminated since the even order optical sidebands are suppressed [19]. Other high-order mixing spurs at $2(f_0 + kt)$, $2f_L$, and $(f_0 + f_L + kt)$ are far beyond the IF range and can be removed simply through filtering. Thus, the wanted IF signal with the frequency of $(f_0 - f_L + kt)$ is obtained with the mixing spurs effectively suppressed. The obtained IF signal is then sent into a digital RFM, which is then sampled, stored, and modulated by an information of $s(t) = \cos[2\pi f_m t + \varphi(t)]$. A reconstructed IF signal is obtained as follows

$$\begin{aligned} \mathrm{IF}_{\mathrm{re}}(t) \propto\ & \cos\left[2\pi(f_0-f_L)t+\pi k t^2\right]\times\cos\left[2\pi f_m t+\varphi(t)\right] \\ =\ & \frac{1}{2}\cos\left[2\pi(f_0-f_L+f_m)t+\pi k t^2+\varphi(t)\right] \\ & +\frac{1}{2}\cos\left[2\pi(f_0-f_L-f_m)t+\pi k t^2-\varphi(t)\right] \end{aligned} \tag{3}$$

The reconstructed IF signal and the LO signal at f_L are applied to the two RF ports of DMZM2 in the lower branch, respectively. DMZM2 is also biased at the minimum transmission point, and only the odd-order optical sidebands remain. Thus, considering the small signal modulation condition, the optical output of

Authorized licensed use limited to: NANJING UNIVERSITY OF AERONAUTICS AND ASTRONAUTICS. Downloaded on February 17,2022 at 06:59:22 UTC from IEEE Xplore. Restrictions apply.

DMZM2 is given as

$$\begin{aligned}E_y(t) = e^{j2\pi f_c t}\Big\{ & e^{j\beta_3 cos\left[2\pi(f_0-f_L+f_m)t+\pi kt^2+\varphi(t)\right]} \\ & \cdot e^{j\beta_3\cos\left[2\pi(f_0-f_L-f_m)t+\pi kt^2-\varphi(t)\right]} \\ & \cdot e^{j\phi_2} + e^{j\beta_4\cos 2\pi f_L t}\Big\} \\ \approx e^{j(2\pi f_c t+\phi_2)}\Big\{ & jJ_1(\beta_3)\, e^{-j\left[2\pi(f_0-f_L+f_m)t+\pi kt^2+\varphi(t)\right]} \\ & + jJ_1(\beta_3)\, e^{j\left[2\pi(f_0-f_L+f_m)t+\pi kt^2+\varphi(t)\right]} \\ & + jJ_1(\beta_3)\, e^{-j\left[2\pi(f_0-f_L-f_m)t+\pi kt^2-\varphi(t)\right]} \\ & + jJ_1(\beta_3)\, e^{j\left[2\pi(f_0-f_L-f_m)t+\pi kt^2-\varphi(t)\right]}\Big\} \\ & + e^{j2\pi f_c t}\left[jJ_1(\beta_4)\, e^{-j2\pi f_L t} + jJ_1(\beta_4)\, e^{j2\pi f_L t}\right]\end{aligned} \tag{4}$$

where β_3 and β_4 are the modulation indices of the input reconstructed IF signal and the LO signal, respectively, and ϕ_2 is the phase difference introduced by the bias voltage applied to DMZM2. The output of DMZM2 is along the Y-polarization axis, and will be output from the other port of the PBS. By injecting the optical signal into PD2, we get

$$\begin{aligned}i_y(t) \propto & +{J_1}^2(\beta_3)\cos\left[4\pi(f_0-f_L+f_m)t+2\pi kt^2+2\varphi(t)\right] \\ & + {J_1}^2(\beta_3)\cos\left[4\pi(f_0-f_L-f_m)t+2\pi kt^2-2\varphi(t)\right] \\ & - J_1(\beta_3)J_1(\beta_4)\cos[2\pi(2f_L-f_0-f_m)t-\pi kt^2 \\ & - \varphi(t)] - J_1(\beta_3)J_1(\beta_4)\cos[2\pi(2f_L-f_0+f_m)t \\ & - \pi kt^2+\varphi(t)] - J_1(\beta_3)J_1(\beta_4)\cos[2\pi(f_0+f_m)t \\ & + \pi kt^2+\varphi(t)] - J_1(\beta_3)J_1(\beta_4)\cos[2\pi(f_0-f_m)t \\ & + \pi kt^2-\varphi(t)]\end{aligned} \tag{5}$$

It can be seen that the LO and RF leakages are effectively suppressed. Other low-frequency mixing spurs of cos[4π(f_0 − f_L + f_m)t + 2πkt^2 + 2φ(t)], cos[4π(f_0 − f_L − f_m)t + 2πkt^2 & 2φ(t)] are far below the RF range and can be removed simply through filtering. Furthermore, the RF mixing spurs including cos[2π(2f_L − f_0 − f_m)t − πkt^2 − φ(t)] and cos[2π(2f_L − f_0 + f_m)t − πkt^2 + φ(t)] have a chirp rate with opposite sign compared to the received RF signal, which will not affect the de-chirp processing or correlation processing between the reference RF signal and the echoes. As a result, a reconstructed RF signal is obtained,

$$\begin{aligned}\mathrm{RF_{re}}(t) \propto & \cos\left[2\pi(f_0+f_m)t+\pi kt^2+\varphi(t)\right] \\ & + \cos\left[2\pi(f_0-f_m)t+\pi kt^2-\varphi(t)\right]\end{aligned} \tag{6}$$

In order to show the jamming capability of the proposed photonics-assisted RFM, the de-chirp processing of the real echo RF signal without interference is performed. The output is

$$\begin{aligned}D_{\mathrm{without}}(t) &\propto \mathrm{LPF}[\mathrm{RF}(t)\times\mathrm{RF}(t-\Delta\tau)] \\ &= \cos\left(2\pi k\Delta\tau t+2\pi f_0\Delta\tau-\pi k\Delta\tau^2\right)\end{aligned} \tag{7}$$

where LPF[] denotes the low bandpass filtering operation, $\Delta\tau$ is the time delay between the reference and the echo. Usually, by performing Fourier analysis upon the de-chirped output signal $D_{\mathrm{without}}(t)$, the distance and velocity information of the target can be obtained [20], [21]. The target distance can be written as $L_\mathrm{y} = c\Delta\tau/2 = cf/2k$, where c is the light velocity in vacuum and $f = k\Delta\tau$. The Doppler frequency shift f_d can be extracted from the phase variation of the microwave carrier preserved by $2\pi f_0\Delta\tau$ between the repeated pulses. Then, the azimuth range can be calculated via $L_\mathrm{x} = \lambda f_d/2\varpi$, where ϖ is the angular speed of the target and λ is the center wavelength of the transmitted radar signal.

As a comparison, when the reconstructed RF signal produced by the proposed photonics-assisted RFM is received by the radar, the de-chirped output should be

$$\begin{aligned}D_{\mathrm{with}}(t) &\propto \mathrm{LPF}[\mathrm{RF}(t)\times\mathrm{RF_{re}}(t-\Delta\tau)] \\ &\propto \cos\left[2\pi\left(k\Delta\tau-f_m\right)t+2\pi\left(f_0+f_m\right)\Delta\tau\right. \\ &\quad \left.-\pi k\Delta\tau^2-\varphi\left(t-\Delta\tau\right)\right] \\ &\quad +\cos\left[2\pi\left(k\Delta\tau+f_m\right)t+2\pi\left(f_0-f_m\right)\Delta\tau\right. \\ &\quad \left.-\pi k\Delta\tau^2+\varphi\left(t-\Delta\tau\right)\right]\end{aligned} \tag{8}$$

As can be seen, two carrier frequencies of $f_1 = k\Delta\tau - f_\mathrm{m}$ and $f_2 = k\Delta\tau + f_\mathrm{m}$ are extracted, leading to two false-target distances of $L_{\mathrm{y}1} = cf_1/2k$ and $L_{\mathrm{y}2} = cf_2/2k$, respectively. The false-target distances can be adjusted by tuning the frequency f_m in the modulated signal s(t). In addition, the phase variations of the two carriers are 2π($f_0 + f_\mathrm{m}$)$\Delta\tau$ − φ(t − $\Delta\tau$) and 2π(f_0 − f_m)$\Delta\tau$ + φ(t − $\Delta\tau$), respectively. Thus, two false azimuth ranges of $L_{\mathrm{x}1} = \lambda f_{d1}/2\varpi$ and $L_{\mathrm{x}1} = \lambda f_{d2}/2\varpi$ are realized, where

$$\begin{cases} f_{\mathrm{d}1} \propto \frac{1}{2\pi}\frac{d[2\pi(f_0+f_m)\Delta\tau-\varphi(t-\Delta\tau)]}{dt} \\ f_{\mathrm{d}2} \propto \frac{1}{2\pi}\frac{d[2\pi(f_0-f_m)\Delta\tau+\varphi(t-\Delta\tau)]}{dt} \end{cases} \tag{9}$$

Because the frequency is determined by the time derivative of the phase function, the phase difference between the transmitted and the received signal is used to estimate the Doppler frequency shift f_d. As shown in Fig. 3, in the delay time (also called fast time) domain, the phase variation may be considered as a constant in one pulse period (0<t<T). While in the pulses (also called slow time) domain, the phase variation would be changed in multiple pulses with the target movement. Thus, the parameters 2π(f_0±f_m)$\Delta\tau$ and φ(t − $\Delta\tau$) in Eq. (9) are related to t in the pulses domain. If the phase φ(t) is given by

$$\varphi(t) = \begin{cases} \varphi_1 = 2\pi & 0 < t < T \\ \varphi_2 = 2\pi+\kappa & T<t<2T \\ \varphi_3 = 2\pi+2\kappa & 2T<t<3T \\ \quad\cdots & \quad\cdots \\ \varphi_N = 2\pi+(N-1)\kappa & (N-1)T<t<NT \end{cases} \tag{10}$$

there would be a fixed phase difference κ between the neighboring radar pulses. As a result, the required azimuth ranges can be flexibly introduced by adjusting the phase φ(t) in the modulated signal s(t). Moreover, by setting the modulated signal s(t) having N carrier frequencies, with the expression of s(t) =

Authorized licensed use limited to: NANJING UNIVERSITY OF AERONAUTICS AND ASTRONAUTICS. Downloaded on February 17,2022 at 06:59:22 UTC from IEEE Xplore. Restrictions apply.

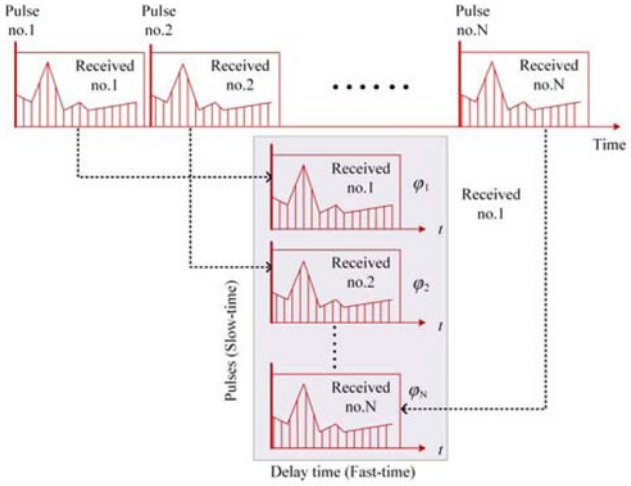

Fig. 3. The received pulse raw data arranged in two dimensions to reflect the concept of fast and slow time [21].

TABLE I
THE MAIN PARAMETERS OF THE SELF-DESIGNED DRFM

Parameters	Value
IF frequency range	0.1-1.1 GHz
Sampling rate	2.5 GSa/s
The quantization bit of ADC	10 bit
The quantization bit of DAC	14 bit
System memory	4 GB

$A_1\cos[2\pi f_{m1}t + \varphi_1(t)] + A_2\cos[2\pi f_{m2}t + \varphi_2(t)] + \ldots + A_N\cos[2\pi f_{mN}t + \varphi_N(t)]$, $2N$ false targets can be produced. In this way, by using the proposed photonics-assisted RFM, multiple false targets with different distances and velocities can be formed.

III. EXPERIMENTAL RESULTS AND DISCUSSION

An experiment is taken based on the scheme shown in Fig. 2. An optical carrier at 1550.54 nm is generated by an LD (TeraXion PureSpectrum-NLL) and divided into two parts through a 50:50 optical power divider. In the experiment, due to the lack of the PM-DMZM, two DMZMs (Fujitsu FTM7937EZ) with a bandwidth of 35 GHz are used and inserted in the two branches, respectively. PD1 (GD45216S) has a 3-dB bandwidth of 18 GHz, and PD2 (Finisar XPDV2120R) has a 3-dB bandwidth of 50 GHz. The LO signal is provided by a microwave source (Agilent E8257D, 250 kHz-67 GHz), and the RF signal is generated by using an arbitrary waveform generator (AWG, Tektronix AWG7001A, 50 GSa/s). The EAs have a frequency range of 2-26.5 GHz and a gain of 27 dB. Two K-band horn antennas with a frequency range of 18-26.5 GHz and a gain of 20 dB are used to emit and receive RF signals. The self-designed DRFM is composed of an ADC, 4-GB memory, a field programmable gate array (FPGA), a DAC, and IF amplifiers. The main parameters of the DRFM module are listed in Table I

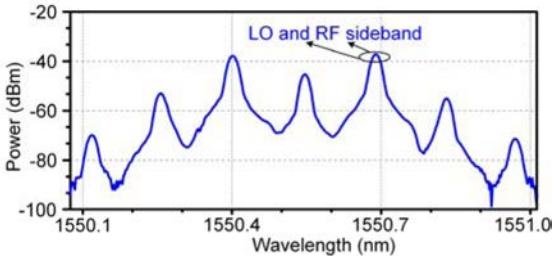

Fig. 4. The optical spectra at the output of DMZM1.

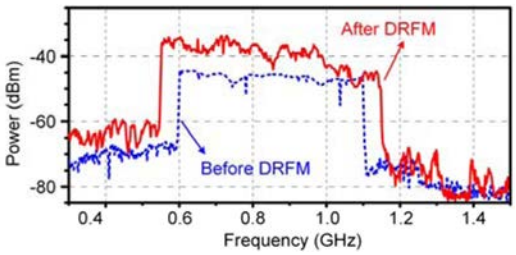

Fig. 5. The electrical spectra of the IF signal before (blue dotted line) and after (red solid line) the digital RFM.

[22, 23]. The optical signals are measured by an optical spectrum analyzer (OSA, YOKOGAWA AQ6370C) with a 0.02-nm resolution, the electrical spectra are observed by an electrical spectrum analyzer (ESA, R&S FSV-40, 10 Hz-40 GHz), and the waveforms are measured by using a real-time oscilloscope (Keysight DSOX93304, 80 GSa/s).

An LFM signal having a frequency range of 17.5–18 GHz, a period of 11 μs and a duty ratio of 90.9% is captured by the received antenna, amplified, and injected into one RF port of DMZM1. A 16.9-GHz LO signal is injected into the other RF port of DMZM1 which is biased at the minimum transmission point. Fig. 4 shows the output optical spectrum. By injecting the optical signal into PD1, a downconverted IF signal covering 0.6–1.1 GHz is obtained, with the electrical spectrum shown as the blue dotted line in Fig. 5. In the digital RFM module, a 50-MHz frequency up-shift and down-shift are introduced to the obtained IF signal, generating two reconstructed IF signals covering 0.55–1.05 GHz and 0.65–1.15 GHz, respectively. The electrical spectrum at the output of the digital RFM is shown as the red solid line in Fig. 5. The amplitude fluctuation of the reconstructed IF signals is mainly due to the response of the used electric IF power amplifiers in the DRFM. It can be further improved by introducing electrical IF amplifiers with better performances.

Then the reconstructed IF signal output from the digital RFM and the 16.9-GHz LO signal are injected into the two RF ports of DMZM2, respectively, with the output optical spectrum shown in Fig. 6. After injecting the optical signal into PD2, a reconstructed RF signal is generated, with the instantaneous frequency to time diagram shown in Fig. 7(a). It can be seen that the generated reconstructed RF signal is composed of two RF LFM signals covering 17.45–17.95 GHz, and 17.55–18.05 GHz, respectively. As a comparison, the instantaneous frequency to time diagram of the input RF signal is given in Fig. 7(b),

Authorized licensed use limited to: NANJING UNIVERSITY OF AERONAUTICS AND ASTRONAUTICS. Downloaded on February 17,2022 at 06:59:22 UTC from IEEE Xplore. Restrictions apply.

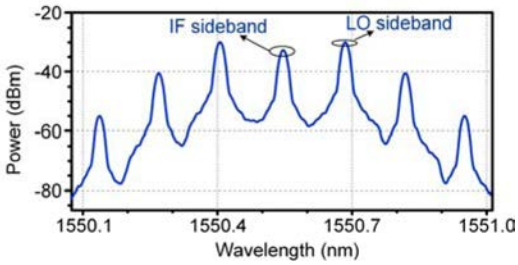

Fig. 6. The optical spectra at the output of DMZM2.

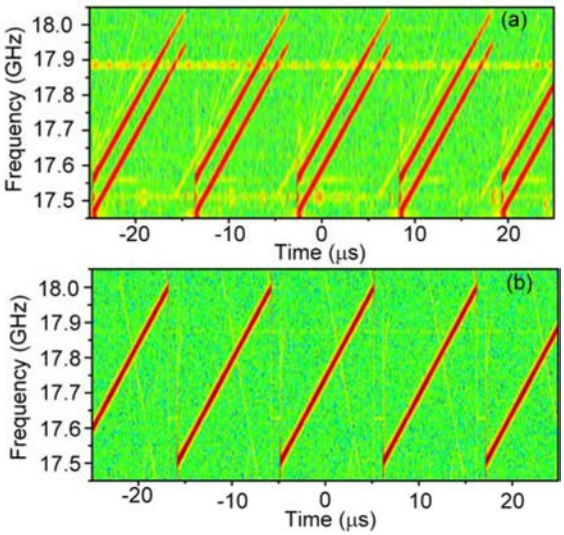

Fig. 7. The instantaneous frequency to time diagrams of (a) the generated reconstructed RF signal and (b) the input RF signal.

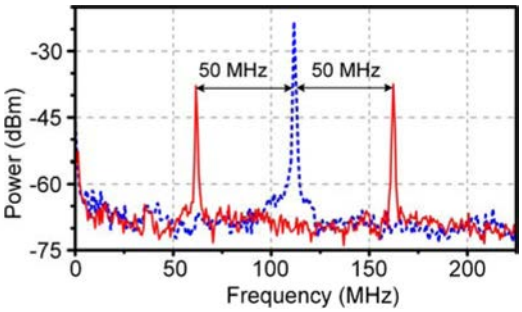

Fig. 8. The electrical spectra of the de-chirped signal before (blue dotted line) and after (red solid line) introducing a ±50-MHz frequency shift.

covering the frequency range of 17.5–18.0 GHz. The frequency components of the reconstructed RF signal have a ±50-MHz frequency shift as compared with the original RF signal.

The reconstructed RF signal is amplified and emitted into the free space through a transmitting antenna, which is received by radar and de-chirped through mixing with the reference RF signal. The de-chirped outputs of the reconstructed RF signal and the original RF signal are shown as the red solid line and the blue dotted line in Fig. 8, respectively. As can be seen, ±50-MHz frequency shift is observed on the de-chirped output of the reconstructed RF signal, as compared with that of the

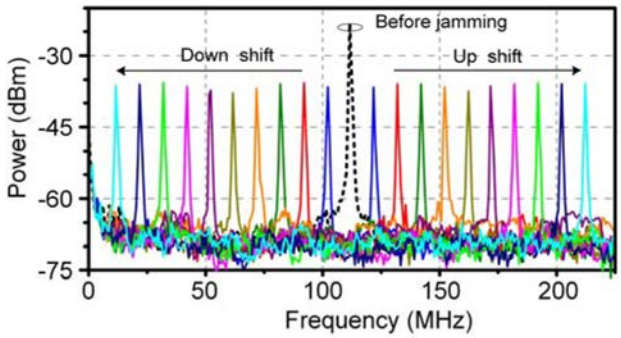

Fig. 9. The electrical spectra of the de-chirped outputs of the original RF signal (black dotted line) and the reconstructed RF signals generated from the photonics-assisted RFM (colorful solid lines).

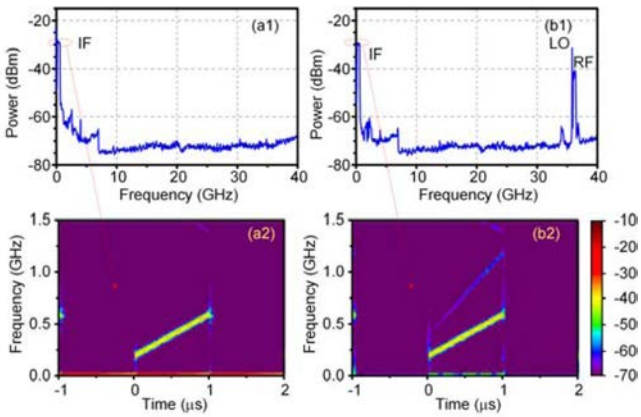

Fig. 10. The (1) electrical spectra and (2) the instantaneous frequency to time diagrams of the downconverted results by using (a) the proposed microwave photonic system and (b) a commercially electrical mixer of Marki M9044L.

original RF signal. Since the target distance of $L = cf/2k$ is estimated according to the de-chirped output with a frequency of f, two false frequency peaks can be considered as two-target scattering points. In this way, the jamming with two false targets is successfully achieved.

The tunability of the proposed photonics-assisted RFM is also investigated. The frequency shift introduced in the digital RFM is tuned from 10 to 100 MHz with a step of 10 MHz. The de-chirped outputs of the corresponding reconstructed RF signals are shown in Fig. 9. According to $L = cf/2k$, the false target distance is expanded to 300 m. Actually, the frequency shift range of the digital RFM can reach 1 GHz. Thus, a false target distance of several km can be achieved.

To show the advantage of mixing spurs suppression, a performance comparison between the used microwave photonic mixing and a commercially available electrical mixer (Marki M9044L) is taken experimentally. The commercial electrical mixer has the RF/LO working frequency range of 4-44 GHz, and the IF working frequency range of up to 3 GHz. An RF LFM signal covering 36–36.4 GHz and a 35.8-GHz LO signal are applied. By using the proposed microwave photonic mixing, the output downconverted electrical spectrum is shown in Fig. 10(a1). As can be seen, for the frequency range of 0–40 GHz, only the desired IF signal covering 0.2–0.6 GHz remains. The

Authorized licensed use limited to: NANJING UNIVERSITY OF AERONAUTICS AND ASTRONAUTICS. Downloaded on February 17,2022 at 06:59:22 UTC from IEEE Xplore. Restrictions apply.

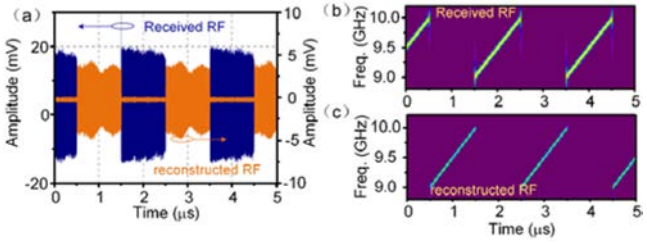

Fig. 11. (a) The waveforms of the received X-band RF signal (in blue line) and the reconstructed RF signal (in brown line). The instantaneous frequency to time diagrams of (b) the received X-band RF signal and (c) the reconstructed RF signal.

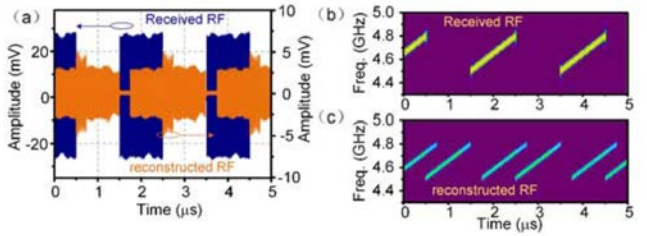

Fig. 12. (a) The waveforms of the received C-band RF signal (in blue line) and the reconstructed RF signal (in brown line). The instantaneous frequency to time diagrams of (b) the received C-band RF signal and (c) the reconstructed RF signal.

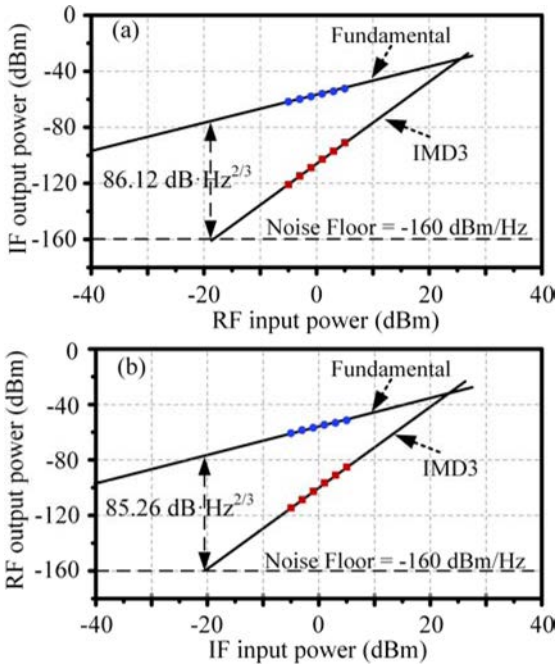

Fig. 13. The measured spurious-free dynamic range (SFDR) performance for (a) the receiving end and (b) the transmitting end when working in the X band.

instantaneous frequency to time diagram of the downconverted result in the IF range of 0–1.5 GHz is shown in Fig. 10(a2). For the commercially available electrical mixer (Marki M9044L), the output electrical spectrum within the frequency range of 0–40 GHz is shown in Fig. 10 (b1). The instantaneous frequency to time diagram in the IF range of 0–1.5 GHz is shown in Fig. 10(b2). It can be seen that the mixing spurs exist, including the RF and LO leakages, and the second harmonic IF components. It should be noted that the second harmonic IF component covers the frequency range of 0.4–1.2 GHz. It is overlapped with the desired IF signal (0.2–0.6 GHz), which can't be removed by filtering. These mixing spurs will constitute a significant feature for jamming recognition. The mixing spurs suppression is vital to the RFM systems for the applications such as radar, electronic warfare, and so on [24]. Thus by using the proposed microwave photonic scheme, the effective mixing spurs suppression can be guaranteed.

The wide operating frequency range of the proposed system is also verified. The operation with the Ka-band RF signal has been shown in Fig. 10(a). The C- and X-band RF signals are also tested. An X-band RF signal covering 9-10 GHz and an 8.9-GHz LO signal are applied. The reconstruction is also applied by introducing a 1-μs time delay. The waveforms of the received RF signal and the reconstructed RF signal are shown in Fig. 11(a) as the blue and brown lines, respectively. The corresponding instantaneous frequency to time diagrams are shown in Fig. 11(b) and (c), respectively. As can be seen, a 1-μs time delay is successfully introduced, which can lead to a false target distance of $L = 150$ m. A C-band RF signal covering 4.5-4.8 GHz and a 4.2-GHz LO signal are also applied. The 0.25-μs and 1-μs time delays are introduced. Fig. 12(a) shows the waveforms of the received C-band RF signal and the reconstructed RF signal, in the blue and brown lines, respectively. Fig. 12(b) and (c) show the corresponding instantaneous frequency to time diagrams. As can be seen, the reconstructed RF signal is composed of two time-delayed RF signals, which would lead to two false target distances of 37.5 m and 150 m, respectively. Thus, the wideband working frequency range from C- to Ka- bands is successfully demonstrated.

The spurious-free dynamic range (SFDR) performance is also investigated experimentally. For the X-band receiving condition, two-tone RF signals with the frequencies of 9.495 and 9.505 GHz are introduced, and the LO signal is set to be 8.9 GHz. The experimentally obtained SFDR value is 86.12 dB·Hz$^{2/3}$, as shown in Fig. 13(a), with the noise floor set to be -160 dBm/Hz. For the X-band transmitting condition, two-tone IF signals with the frequencies of 0.995 and 1.005 GHz are applied, with the LO signal kept being 8.9 GHz. The SFDR is measured to be 85.26 dB·Hz$^{2/3}$, as shown in Fig. 13(b). The SFDR performances for the Ku-band working condition are shown in Fig. 14. As shown in Fig. 14(a), the SFDR of 82.81 dB·Hz$^{2/3}$ is obtained for the receiving end, through the two-tone test by using two-tone RF signals of 17.795 and 17.805 GHz and a 16.9-GHz LO. By applying two-tone IF signals with the frequencies of 0.995 and 1.005 GHz, and a 16.9-GHz LO, the obtained SFDR for the Ku-band transmitting end is 80.78 dB·Hz$^{2/3}$, as shown in Fig. 14(b). As can be seen, the SFDR values of larger than 80 dB·Hz$^{2/3}$ are obtained for all the conditions. The experimentally obtained SFDR performances are limited by the characteristics of the used devices in the experiments, especially the DMZMs. The SFDR performances can be further improved by using DMZMs with better characteristics, including a higher extinction ratio, a smaller half-wave voltage, and a wider working frequency.

Authorized licensed use limited to: NANJING UNIVERSITY OF AERONAUTICS AND ASTRONAUTICS. Downloaded on February 17,2022 at 06:59:22 UTC from IEEE Xplore. Restrictions apply.

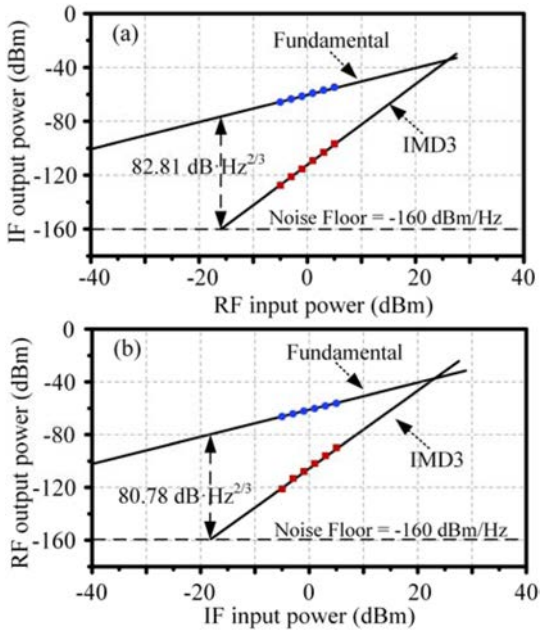

Fig. 14. The measured SFDR performance for (a) the receiving end and (b) the transmitting end when working in the Ku band.

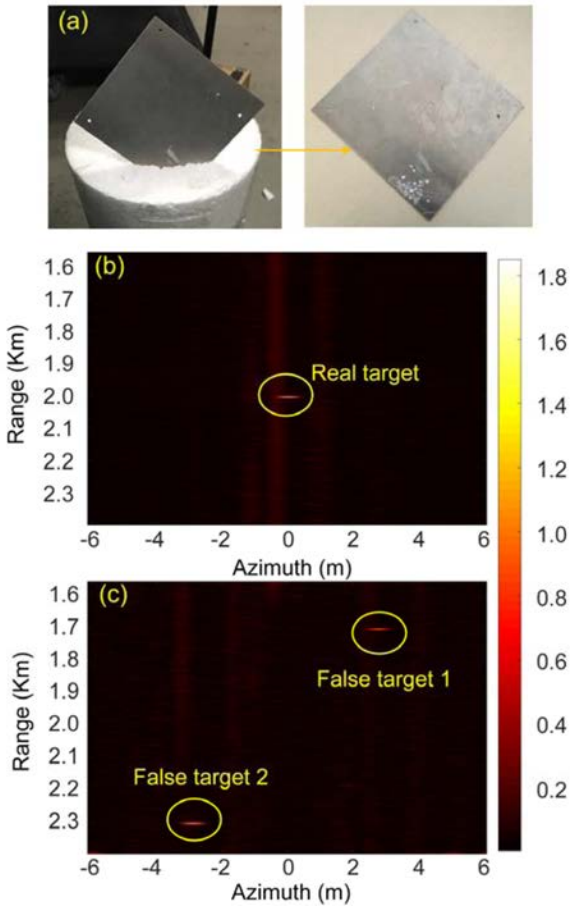

Fig. 15. Demonstration of the multiple false targets jamming to deceive the radar imaging by using the proposed photonics-assisted RFM. (a) Photograph of the target placed at a turntable. The imaging results (b) without and (c) with jamming.

To further investigate the performance of the proposed photonics-assisted RFM system, an experiment to deceive the radar inverse synthetic aperture radar (ISAR) imaging is performed. The initial RF signal for emitting is an LFM signal with a bandwidth of 500 MHz centered at 17.75 GHz and a temporal period of 100 μs (100% duty ratio). A planar reflector with a size of 18 cm $\times$ 19 cm placed at a turntable is used as the target, as shown in Fig. 15(a). The turntable is rotating in the horizontal plane, whose angular speed is 2π rad/s. Without introducing the photonics-assisted RFM, the ISAR imaging result with the target is shown in Fig. 15(b). The real target distance is limited to about 1 m when operating in the lab. To show the ISAR imaging with a km-range false target, a system delay is added by inserting fibers to make the reference range of the real target to be 2 km. By introducing the photonics-assisted RFM, a reconstructed RF signal will be generated, and the achieved image is shown in Fig. 15(c). As can be seen, two false targets are successfully inserted based on the proposed photonics-assisted RFM. By introducing a 10-MHz frequency shift, a 300-m displacement in the longitudinal distance is achieved. Besides, a $0.21 \times 2\pi$ phase difference between adjacent radar pulses is applied to achieve a 2.8-m displacement in the azimuth range.

IV. Conclusion

In conclusion, a photonics-assisted RFM has been proposed and demonstrated. By combing the wideband microwave photonic mixer and flexible digital RFM, the wide working frequency range from C- to Ka- bands is achieved. The mixing spurs are effectively suppressed, and flexible modulation and time delay manipulations are achieved. Two false targets are experimentally realized to deceive a K-band radar imaging. The simplicity of the scheme is guaranteed since only one PM-DMZM is needed. The operational frequency range of the system can be further extended by using electro-optic modulators and PDs with wider working frequency ranges. With the increasing complexity of the electromagnetic environment, the mixing spurs with the RFMs will be more complex. The proposed scheme can suppress the mixing spurs of the second harmonic IF components and the RF and LO leakages. By further introducing photonics-based advanced mixing functions [19], such as the image rejection mixing techniques [25], the mixing spurs such as the image can also be suppressed to further improve the system performance. In addition, by introducing a microwave photonic channelizer structure [26], the instantaneous working bandwidth can be effectively extended. With the fast development of microwave photonic integration techniques [27], the integration of the system can be achieved. The proposed scheme shows great potential in the applications of electronic warfare, electronic environment simulation and testing, and so on.

References

[1] S. J. Roome, "Digital radio frequency memory," *Electron. Commun. Eng. J.*, vol. 2, no. 4, pp. 147–153, 1990.

[2] Q. Cheng, Z. H. Shi, P. Dong, and B. L. He, "Application of DRFM in high frequency ground wave radar," in *Proc. 6th Int. Conf. ASIC*, 2005, pp. 774–777.

Authorized licensed use limited to: NANJING UNIVERSITY OF AERONAUTICS AND ASTRONAUTICS. Downloaded on February 17,2022 at 06:59:22 UTC from IEEE Xplore. Restrictions apply.

[3] C. M. Kwak, "Application of DRFM in ECM for pulse type radar," in *Proc. 34th Int. Conf. Infrared Millimeter Terahertz Waves*, pp. 1–2, 2009.
[4] M. Soumekh, "SAR-ECCM using phase-perturbed LFM chirp signals and DRFM repeat jammer penalization," *IEEE Trans. Aerosp. Electron. Syst.*, vol. 42, no. 1, pp. 191–205, Jan. 2006.
[5] A. Kale, R. Thirumuru, and V. S. R. Pasupureddi, "Wideband channelized sub-sampling transceiver for digital RF memory based electronic attack system," *Aerosp. Sci. Technol.*, vol. 51, pp. 34–41, 2016.
[6] C. P. Heagney, "Digital radio frequency memory synthetic instrument enhancing US navy automated test equipment mission," *IEEE Instrum. Meas. Mag.*, vol. 21, no. 4, pp. 41–63, Aug. 2018.
[7] P. Ghelfi *et al.*, "A fully photonics-based coherent radar system," *Nature*, vol. 507, pp. 341–345, 2014.
[8] S. L. Pan and Y. M. Zhang, "Microwave photonic radars," *J. Lightw. Technol.*, vol. 38, no. 19, pp. 5450–5484, 2020.
[9] K. Davidson and J. Bray, "Understanding digital radio frequency memory performance in countermeasure design," *Appl. Sci.*, vol. 10, no. 12, 2020, Art. no. 4123.
[10] C. C. Lessi *et al.*, "GaN-AlGaN on SiC pHEMT design for a digital radio frequency memory," in *Proc. IEEE 28th Int. Conf. Mixed. Des. Integr. Circuits Syst.*, 2021, pp. 100–103.
[11] B. Manz, "DRFM grow to meet new threats," *J. Electron. Defense*, vol. 33, no. 8, pp. 43–48, 2010.
[12] O. Ozdil, A. Yildirim, M. Ispir, and I. E. Ortatatli, "Channelized DRFM for wideband signals," in *Proc. Int. Radar Conf.*, 2016, pp. 1–5.
[13] J. Capmany and D. Novak, "Microwave photonics combines two worlds," *Nature Photon.*, vol. 1, pp. 319–330, 2007.
[14] L. V. T. Nguyen, "Photonic radio frequency memory—Design issues and possible solutions," *Defence Sci. Technol. Organisation*, Edinburgh, Scotland, Tech. Rep. DSTO-TR-1491, 2003.
[15] T. A. Nguyen, E. H. W. Chan, and R. A. Minasian, "Photonic radio frequency memory using frequency shifting recirculating delay line structure," *J. Lightw. Technol.*, vol. 32, no. 1, pp. 99–106, 2014.
[16] Z. D. Ding *et al.*, "Photonic high-fidelity storage and doppler frequency shift of broadband RF pulse signals," *Opt. Exp.*, vol. 27, no. 23, pp. 34359–34369, 2019.
[17] Z. D. Ding *et al.*, "Multifunctional photonic broadband RF memory for complex electronic jamming," *Laser Phys. Lett.*, vol. 17, paper. 116201-1-8, 2020.
[18] D. Zhu and S. L. Pan, "Broadband cognitive radio enabled by photonics," *J. Lightw. Technol.*, vol. 38, no. 12, pp. 3076–3088, 2020.
[19] Z. Z. Tang, Y. F. Li, J. P. Yao, and S. L. Pan, "Photonics-based microwave frequency mixing: Methodology and applications," *Laser Photon. Rev*, vol. 14, no. 1, paper. 1800350-1-25, 2020.
[20] O. Caner, *Inverse Synthetic Aperture Radar Imaging With MATLAB Algorithms*. Hoboken, NY, USA: Wiley, 2012.
[21] V. C. Chen and M. Martorella, *Inverse Synthetic Aperture Radar Imaging: Principles, Algorithms and Applications*. Raleigh, NC, USA: SciTech Publishing, 2014.
[22] L. Wang, "Research on low-spurious and wide-band digital radio frequency memory system," Master's thesis, Nanjing Univ. Aeronaut. Astronaut., 2015.
[23] P. Chen, "Design and experimental of digital radio frequency memory system," Master's thesis, Nanjing Univ. Aeronaut. Astronaut., 2018.
[24] K. Olivier, J E Cilliers, and Plessis M. Du, "Design and performance of wideband DRFM for radar test and evaluation," *Electron. Lett.*, vol. 47, no. 14, pp. 824–925, 2011.
[25] D. Zhu and S. L. Pan, "Photonics-based microwave image-reject mixer," *MDPI Photon.*, vol. 5, no. 2, pp. 6-1-12, Mar. 2018.
[26] W. J. Chen, D. Zhu, C. X. Xie, J. Liu, and S. L. Pan, "Microwave channelizer based on a photonic dual-output image-reject mixer," *Opt. Lett.*, vol. 44, no. 16, pp. 4052–4055, 2019.
[27] D. Marpaung, J. Yao, and J. Capmany, "Integrated microwave photonics," *Nature Photon.*, vol. 13, pp. 80–90, 2019.

Dan Zhu (Member, IEEE) received the B.S. and Ph.D. degrees in electronic engineering from Tsinghua University, Beijing, China, in 2004 and 2009, respectively. In May 2011, she joined the College of Electronic and Information Engineering, Nanjing University of Aeronautics and Astronautics, Nanjing, China, where she is currently a Full Professor. From May 2014 to May 2015, she was a Visiting Scholar with the Microwave Photonics Research Laboratory, University of Ottawa, Ottawa, ON, Canada. Her current research interests include microwave photonic signal processing and the system applications. Dr. Zhu is a Member of the IEEE Microwave Theory and Techniques Society, the IEEE Photonics Society, and the Optical Society of America.

Wenjuan Chen received the B.S. degree in 2016 in electronic science and technology from the Nanjing University of Aeronautics and Astronautics, Nanjing, China, where she is currently working toward the Ph.D. degree. Her research interests include photonic signal processing and photonics-based RF front-end.

Sijia Liu received the B. S. degree in electromagnetic field and microwave technology from the Nanjing University of Posts and Telecommunications, Nanjing, China, in 2017. He is currently working toward the Ph.D. degree with the Nanjing University of Aeronautics and Astronautics, Nanjing, China. His research interests include RF simulation and radar signal processing.

Yue Yang received the B.S. degree in 2018 from the Nanjing University of Aeronautics and Astronautics, Nanjing, China, where he is currently working toward the Ph.D. degree with the Key Laboratory of Radar Imaging and Microwave Photonics, Ministry of Education. His main research interests include photonics-based radars for high-resolution imaging and photonics-based array imaging.

Jiang Liu received the B.S. degree in 2018 in electronic science and technology from the Nanjing University of Aeronautics and Astronautics, Nanjing, China, where he is currently working toward the M.S. degree. His research focuses on microwave photonic processing.

Xingwei Ye (Student Member, IEEE) received the B.S. degree from the Nanjing University of Aeronautics and Astronautics, Nanjing, China, in 2014 and the Ph.D. degree in 2020. His main research interests include photonic technologies for RF beamforming, synthetic aperture imaging, and direct sampling.

Minghai Pan received the M.S. and Ph.D. degrees from the Harbin Institute of Technology, Harbin, China, in 1988 and 2000, respectively. In 2005, he joined the College of Electronic and Information Engineering, Nanjing University of Aeronautics and Astronautics, Nanjing, China, where he is currently a Full Professor. His research focuses on microwave technology for radar applications.

Shilong Pan (Senior Member, IEEE) received the B.S. and Ph.D. degrees in electronic engineering from Tsinghua University, Beijing, China, in 2004 and 2008, respectively. From 2008 to 2010, he was a "Vision 2010" Postdoctoral Research Fellow with the Microwave Photonics Research Laboratory, University of Ottawa, Ottawa, ON, Canada. In 2010, he joined the College of Electronic and Information Engineering, Nanjing University of Aeronautics and Astronautics, Nanjing, China, where he is currently a Full Professor and an Executive Director of the Key Laboratory of Radar Imaging and Microwave Photonics, Ministry of Education. He has authored or coauthored more than 420 research papers, including more than 240 papers in peer-reviewed journals and 190 papers in conference proceedings. His research focuses on microwave photonics, which includes optical generation and processing of microwave signals, analog photonic links, photonic microwave measurement, and integrated microwave photonics. Prof. Pan is currently an Associate Editor of the Electronics Letters, a Topical Editor of Chinese Optics Letters, and is a Technical Committee Member of IEEE MTT-3 Microwave Photonics. He has also served as a Chair of number of international conferences, symposia, and workshops, including the TPC Chair of the International Conference on Optical Communications and Networks in 2015 and TPC Co-Chair of IEEE International Topical Meeting on Microwave Photonics in 2017. Prof. Pan is a Fellow of OSA, SPIE, and IET. In 2019, he was selected as an IEEE Photonics Society Distinguished Lecturer.

uthorized licensed use limited to: NANJING UNIVERSITY OF AERONAUTICS AND ASTRONAUTICS. Downloaded on February 17,2022 at 06:59:22 UTC from IEEE Xplore. Restrictions apply